

# Bubble nucleation and gravitational wave from holography

Yidian Chen,<sup>1,\*</sup> Danning Li,<sup>2,†</sup> and Mei Huang<sup>1,‡</sup>

<sup>1</sup>*School of Nuclear Science and Technology, University of Chinese Academy of Sciences, Beijing 100049, P.R. China*

<sup>2</sup>*Department of Physics and Siyuan Laboratory, Jinan University, Guangzhou 510632, P.R. China*

We investigate the bounce solution in the holographic QCD and electroweak models with first-order phase transition. The strength parameter  $\alpha$ , inverse duration time  $\beta/H$  and bubble wall velocity  $v_w$  in the gravitational wave power spectra are calculated by holographic bounce solution. In contrast to the results of field theory, we find the parameter  $\alpha$  is about  $\mathcal{O}(1)$  and  $\beta/H$  is about  $10^4$ , which imply that the phase transition is fast and strong. The critical, nucleation and percolation temperatures of the phase transition are close to each other in the holographic model. In addition, the velocity  $v_w$  is found to be less than the sound speed of the plasma  $c_s = 1/\sqrt{3}$ , which corresponds to the deflagration scenario. For QCD phase transition, the gravitational wave power spectrum can reach  $10^{-13} - 10^{-14}$  around the peak frequency of 0.01 Hz, which can be detected by BBO and Ultimate-DECIGO. For electroweak phase transition, the gravitational wave power spectrum can reach  $10^{-12} - 10^{-16}$  around the peak frequency 1 – 10 Hz. Moreover, the primordial black hole is not favorable for formation due to the large parameter  $\beta/H$  and small velocity  $v_w$ .

## I. INTRODUCTION

Gravitational waves (GWs) are one of the great predictions of general relativity [1, 2], which exhibits an effect of the curvature of spacetime. In 1974, Hulse and Taylor discovered the binary system PSR 1913+16 [3], providing indirect evidence for the existence of GWs, for which they received the 1993 Nobel Prize in Physics. In 2015, astronomy entered the multi-messenger era with the first observation of a gravitational wave event by LIGO [4, 5]. Nowadays, more and more GW events or possible GW signals are discovered, as in Refs. [6], which also provide new instruments for understanding cosmology and astronomy deeply.

The GWs come from the quadrupole moment radiation of the stress-energy tensor, which can be roughly classified into two categories, that is, cosmological and astronomical sources (see the reviews Refs. [7–9]). The stochastic GW background generated by the first-order phase transition (FOPT) of the early universe is a significant cosmological source of GWs (see the reviews Ref. [10]). Different from the transient GWs observed at the present, the stochastic GW background comes from all directions rather than specific ones.

The detection experiments of GWs mainly include ground-based experiments, space-based experiments, pulsar timing arrays (PTA), and cosmic microwave background polarization, (see [11] for review). The ground-based experiments, such as LIGO [12], Virgo [13], Einstein Telescope (ET) [14], Cosmic Explorer (CE) [15], etc., mainly observe compact binary systems. The space-based experiments, such as Laser Interferometer Space Antenna (LISA) [16], Deci-Hertz Interferometer Gravitational wave Observatory (DECIGO) [17, 18], Big Bang Observer (BBO) [19], Taiji [20], Tianqin [21], etc., are more sensitive to the GWs from electroweak phase transition. The PTAs, such as the Parkes PTA (PPTA) [22], the European PTA (EPTA) [23], the North American Nanohertz Observatory for Gravitational Waves (NANOGrav) [24], the International PTA (IPTA) [25] and the Chinese PTA (CPTA), etc., are mainly sensitive to the GWs from QCD phase transitions.

The dynamic process of the FOPT is described by bubble dynamics. When the temperature of the system reaches the critical temperature  $T_c$  for the phase transition, it does not immediately enter the symmetric broken phase since the generation of true vacuum bubbles causes additional surface free energy, which increases the total free energy of the system. As the temperature decreases to the nucleation temperature  $T_n$ , bubbles are more likely to be generated due to the increasing probability of thermal perturbation or quantum tunneling that crosses the free energy barrier. The temperature drops further to the percolation temperature  $T_p$ , and more than one-third of the space enters into the true vacuum. During this process, the bubble expands continuously since the internal pressure is greater than the false vacuum pressure and surface tension, and it may eventually reach the final velocity because of the friction of the plasma or accelerate to near the speed of light. Throughout the process, collisions of bubbles, acoustic modes of the plasma and turbulences of the magnetohydrodynamics all generate GWs and eventually contribute to the GW power spectra.

---

\* chenyardian@ucas.ac.cn

† lidanning@jnu.edu.cn

‡ huangmei@ucas.ac.cn

During the evolution of the universe, it may undergo various phase transitions, such as grand unification phase transition, electroweak phase transition (EWPT), and QCD phase transition (QCDPT). The FOPT is of interest since it is related to some physical processes such as baryogenesis, the seeds of intergalactic magnetic fields and the formation of primordial black holes. Unfortunately, the electroweak part of the standard model is crossover [26–28], while the Lattice QCD calculations indicate that the QCD phase transition of the three flavors is crossover at zero chemical potential and finite temperature [29, 30]. Of course, many new physical models beyond the standard model (BSM) predict the FOPT, such as the two-Higgs doublet model [31–33], the left-right symmetric model [34], the technicolor model [35–37], etc. In addition, since QCDPT is flavor-dependent, there is still the possibility of a first-order QCDPT.

The discovery of the anti-de Sitter/conformal field theory (AdS/CFT) correspondence [38–40] has provided a new way to solve strongly coupled field theory calculations. In the past two decades, holographic QCD has been widely studied both in top-down [41–43] and bottom-up models [44–50]. For beyond the standard model the technicolor model [51–56] and composite Higgs model [57–60] have been extended to the holographic framework.

The intensity of the GW signal is impacted by the strength of the phase transition, its duration time and the final velocity of the bubble wall. The calculations in weakly coupled quantum field theory suggest that the strength parameter  $\alpha$  is roughly  $\alpha \sim 0.01$  and the inverse of the duration time  $\beta/H$  is roughly  $\beta/H \sim 100$  during EWPT. As for the speed, one would expect that it is close to the speed of light  $c$  for enhancing the GW signal. These quantities are not sufficiently discussed and understood when the system is strongly coupled. The holographic principle provides new ways to explore the thermodynamic and kinetic properties of phase transitions with strong coupling. The bubble nucleation dynamics [61–72] and the GW power spectra [54, 73–79] are considered in the holographic model. The relation between the bubble velocity and the pressure difference of the true and false vacuum is investigated in Refs. [63, 65, 72]. In Refs. [69, 70], the profile of the fluid velocity is calculated inside and outside the bubble wall.

The paper is organized as follows. The five-dimensional holographic QCD and electroweak models are introduced in Sec. II. In Sec. III, the bounce solution and bubble wall velocity are obtained in the holographic model. Using the bounce solution, the properties of the critical bubble and the thin-wall approximation are considered in Sec. IV. In Sec. V, the stochastic GW power spectra generated by the strongly coupled FOPT are calculated. Finally, the conclusion and discussion are presented in Sec. VI.

## II. 5D SETUP

In this section, we consider FOPT of QCD or QCD-like electroweak theories, which corresponds to  $SU(N_f)_L \times SU(N_f)_R$  flavor symmetry breaking to  $SU(N_f)_V$  subgroup. Here, only the scalar part of the flavor-brane is considered under the probe approximation, which has the following form

$$S = - \int d^5x \sqrt{-g} e^{-\Phi} \text{Tr}[(D^M X)^\dagger (D_M X) + V_X(|X|)]. \quad (1)$$

Among this,  $\Phi$  denotes the dilaton field and the complex scalar field  $X$  corresponds to the quark condensation  $\langle \bar{q}q \rangle$  or fermionic condensate of BSMs. The symmetry of the model is spontaneously broken by the non-zero vacuum expectation value of the scalar field  $X = \frac{\chi(z,x)}{\sqrt{2N_f}} I_{N_f}$ , where  $I_{N_f}$  is the  $N_f \times N_f$  identity matrix and  $\chi$  depends not only on the fifth coordinate  $z$  but also on the four-dimensional space-time coordinates  $x^\mu$ .

In this paper, the back-reaction of the dilaton field  $\Phi$  and the scalar field  $X$  are not taken into account, so the background geometry remains the AdS<sub>5</sub>-Schwarzschild black brane metric

$$ds^2 = \frac{L^2}{z^2} [-f(z)dt^2 + \frac{1}{f(z)}dz^2 + dx_i dx^i], \quad (2)$$

with the blackening factor  $f(z) = 1 - \frac{z_h^4}{z^4}$  and the horizon  $z_h$ . For convenience, the AdS radius  $L$  is set to 1 in the following. The Hawking temperature of the system is

$$T = \frac{|f'(z)|}{4\pi} = \frac{1}{\pi z_h}. \quad (3)$$

In order to realize the FOPT, the potential of the scalar field is considered to have the following form [80–82]

$$V(\chi) \equiv \text{Tr}[V_X(|X|)] = \frac{M_5^2}{2} \chi^2 + v_3 \chi^3 + v_4 \chi^4 + v_6 \chi^6, \quad (4)$$

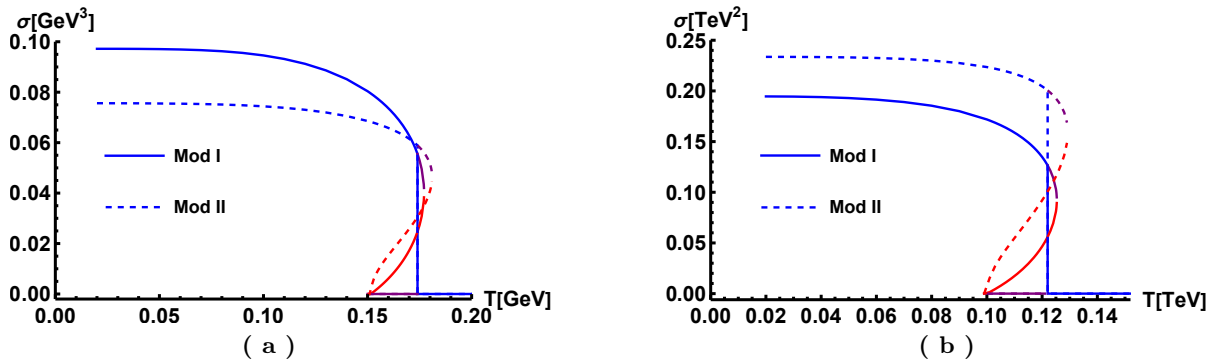


Figure 1. The condensate  $\sigma$  as a function of temperature  $T$ . Panels (a) and (b) correspond to the QCD and EW cases, respectively.

where  $M_5^2$  denotes the square of the five-dimensional mass, and  $v_3$ ,  $v_4$  and  $v_6$  are the cubic, quadratic and sextic terms coupling constants, respectively. According to the AdS/CFT dictionary, the five-dimensional mass of the scalar field  $X$  is  $M_5^2 = (\Delta - p)(\Delta + p - 4) = -3$  by taking  $p = 0$  and  $\Delta = 3$  for QCD. For the EW model, a large anomalous dimension  $\gamma_m \simeq 1$  needs to be considered[83–88], so the five-dimensional mass is  $M_5^2 = (\Delta - \gamma_m)(\Delta - \gamma_m - 4) = -4$  by taking  $\Delta = 3$  and  $\gamma_m = 1$ . For simplicity, we do not consider all nonzero nonlinear terms, but instead consider two special cases, i.e.,  $v_6 = 0$  (Model I) or  $v_3 = 0$  (Model II). The correct chiral symmetry breaking in the chiral limit depends on the form of the dilaton field, which is chosen as in Refs. [80, 81]

$$\Phi = -\mu_1 z^2 + (\mu_1 + \mu_0) z^2 \tanh(\mu_2 z^2), \quad (5)$$

where the  $\mu_0$ ,  $\mu_1$ , and  $\mu_2$  parameters determine the behavior of the dilaton field in the IR and UV.

In this holographic model, five free parameters  $[\mu_0, \mu_1, \mu_2, v_3, v_4]$  or  $[\mu_0, \mu_1, \mu_2, v_4, v_6]$  are included. For the QCD case, we choose  $[\mu_0, \mu_1, \mu_2, v_3, v_4] = [(0.43\text{GeV})^2, (0.83\text{GeV})^2, (0.176\text{GeV})^2, -3, 8]$  (Model I) or  $[\mu_0, \mu_1, \mu_2, v_4, v_6] = [(0.43\text{GeV})^2, (0.83\text{GeV})^2, (0.176\text{GeV})^2, -12, 100]$  (Model II) with the critical temperature of the phase transition  $T_c \simeq 174$  MeV, by referring to Refs. [80–82]. For the EW case,  $\mu_0 = \mu_2 = 0$  is chosen to simplify the model. It is worth noting that if  $\Phi = -\mu_1 z^2$  is chosen, there is an additional massless scalar meson in the particle spectra, as in Ref. [89]. For QCD, this is nonphysical. However, for the EW, this state can be interpreted as the Higgs boson, which obtains mass by interacting with other scalar fields. Therefore, for the EW case, the parameters are chosen as  $[\mu_0, \mu_1, \mu_2, v_3, v_4] = [0, (0.28\text{TeV})^2, 0, -1.1, 3]$  (Model I) or  $[\mu_0, \mu_1, \mu_2, v_4, v_6] = [0, (0.28\text{TeV})^2, 0, -1.8, 4]$  (Model II) with critical temperatures of  $T_c \simeq 122$  GeV. The Panels. (a) and (b) of Fig. 1 show the QCD and technicolor condensate as a function of temperature, respectively. In fact, the specific values of these parameters do not affect the qualitative results in the following sections. In principle, the same approach can be used for symmetry breaking of other groups, simply by changing the representation of the group.

### III. BOUNCE SOLUTION AND BUBBLE VELOCITY

In this section, we will study the kinetics of the FOPT in the holographic model, which will involve the thermodynamics and dynamics of the bubble, describing how the phase transition occurs and how long the phase transition lasts. The phase transition kinetics are characterized by nucleation temperature, latent heat, transition rate parameters, bubble velocity, etc., which will determine the specific magnitude of the GW spectrum.

The kinetic process of the FOPT is described by the nucleation theory, in which the creation, expansion and fusion of bubbles transform the false vacuum  $\chi_f$  into the true vacuum  $\chi_t$ . The bubble nucleation is caused by quantum tunneling or thermal perturbation. At the critical temperature  $T_c$ , the true and false vacuums have the same free energy, and the phase transition is suppressed due to the surface free energy of the bubbles increasing the total free energy of the system. As the temperature decreases, the difference between the free energy of the true and false vacuum compensates for the surface free energy, and the bubble generation becomes more and more probable until the phase transition is completed.

In the first half of the 20th century, classical and modern nucleation theories were established[90, 91]. In the 1970s, nucleation theory was extended to relativistic quantum field theory by Coleman and Callan[92, 93], while in Refs. [94–97] and [98] it was further extended to finite temperature and density, respectively. See Refs. [99–101] for some reviews.

### A. Bounce Solution

In this subsection, we will construct bubble solutions in the holographic model. Considering the spherical symmetry of the bubble, the AdS-Schwarzschild metric is rewritten in spherical coordinates

$$ds^2 = \frac{1}{z^2}[-f(z)dt^2 + \frac{1}{f(z)}dz^2 + dr^2 + r^2d\theta^2 + r^2\sin^2\theta d\varphi^2], \quad (0 \leq r \leq R) \quad (6)$$

with azimuth  $\varphi$ , zenith angle  $\theta$  and the edge  $R$ . Then, the equations of motion of the scalar field  $X$  can be obtained from action (1)

$$\partial_r^2 \chi(z, r) + \frac{2\partial_r \chi(z, r)}{r} + f(z)\partial_z^2 \chi(z, r) + \left(f'(z) - f(z)\Phi'(z) - \frac{3f(z)}{z}\right)\partial_z \chi(z, r) - \frac{\partial_\chi V(\chi)}{z^2} = 0. \quad (7)$$

Coleman and Callan[92, 93] proposed that the critical bubble is described by the bounce solution in quantum nucleation theory. The solution requires the following boundary conditions

$$\lim_{r \rightarrow \infty} \chi(z, r) = \chi_f, \quad (8)$$

$$\left. \frac{d\chi(z, r)}{dr} \right|_{r=0} = 0. \quad (9)$$

For the fifth dimensional direction, the expansion of the scalar field  $\chi$  at the conformal boundary has the following form

$$\chi|_{z \rightarrow 0} = m_q \zeta z + \dots + \frac{\sigma}{\zeta} z^3 + \dots \quad (\text{QCD}), \quad (10)$$

$$= \sigma z^2 + \dots \quad (\text{EW}), \quad (11)$$

with the quark current mass  $m_q$ , the condensate  $\sigma$  and constant  $\zeta = \frac{\sqrt{N_c}}{2\pi}$ . Here, we keep the terms related with the 4D operators only, and in the following calculation we will take  $N_c = 3$  for the QCD case. Since the FOPT is considered, it is convenient to set the current mass  $m_q$  to 0. At the IR boundary, the natural boundary condition is selected. Under saddle point approximation, the tunneling rate of the stochastically generated bubbles is

$$\Gamma(T) = A(T)e^{-\frac{S_b}{T}}, \quad (12)$$

where  $S_b$  is the Euclidean action evaluated on the bounce solution and the factor is  $A = T^4(\frac{S_b}{2\pi T})^{3/2}$ [95, 96]. According to the holographic principle, the partition function has the equivalence  $\mathcal{Z}_{\text{QFT}} \simeq \mathcal{Z}_{\text{Gra}}$ , so the action  $S_b$  can be calculated by the gravitational part  $S_b \simeq S_5$ . The Euclidean action of the bounce solution has the following form

$$S_b \simeq S_5 = 4\pi \int_0^R dr \int_0^{z_h} dz \sqrt{-g} e^{-\Phi(z)} \left(-\frac{v_3}{2} \chi^3 - v_4 \chi^4 - 2v_6 \chi^6\right). \quad (13)$$

By solving the equation of motion Eq. (7) with the boundary conditions Eqs. (8-11), we can obtain the bounce solution in the holographic model. For simplicity, we focus on the case of the QCD phase transition with  $v_3 \neq 0$  (Model I). For other parameter values or holographic EW models, the qualitative conclusions do not change. The panel (a) of Fig. (2) shows the scalar field  $\chi$  as a function of the fifth dimensional coordinate  $z$  and the radial coordinate  $r$  at a temperature of 172 MeV. It can be seen that the scalar field  $\chi$  has a nontrivial structure as a function of  $z$  when the radial  $r$  is small, while the profile of  $\chi$  varies continuously to the trivial solution as  $r$  tends to the edge  $R$ .

The panel (b) of Fig. 2 represents the condensation as a function of radial  $r$  at different temperatures. It can be seen that the size of the critical bubble diminishes with decreasing temperature. As the temperature decreases, the free energy barrier between the true and false vacuums is reduced, and small-size bubbles are more likely to form. It should be noted that the condensation values at the center of the bubble do not reach the equilibrium values when  $T \lesssim 170$  MeV. This can be interpreted as the fact that at that temperature, the bubbles are composed mainly of bubble walls, as can be seen from panel (b) of Fig. 2. The true vacuum is revealed inside the bubble when  $T \gtrsim 170$  MeV.

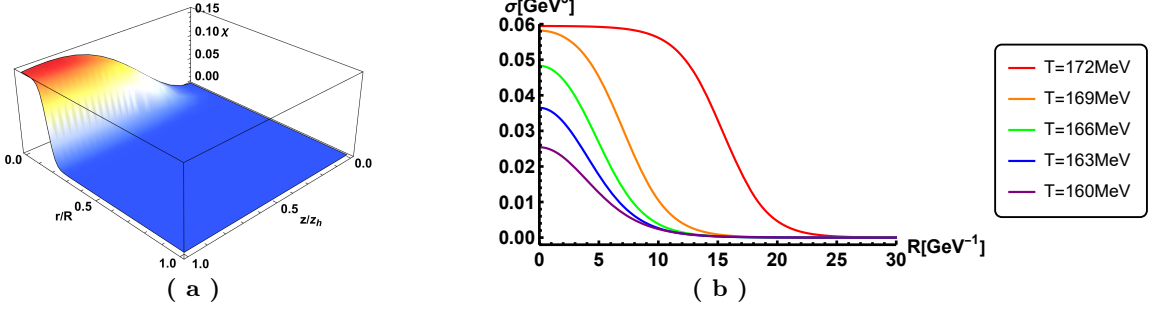


Figure 2. The panel (a) represents the bounce solution of the scalar field  $\chi_b$  as a function of the fifth dimensional coordinate  $z$  and the radial coordinate  $r$ . The panel (b) indicates the condensate  $\sigma$  as a function of the radial coordinate  $r$  at different temperatures.

### B. Bubble velocity

When a large enough bubble is created in the plasma, it expands, collides with each other and eventually transforms the false vacuum into a true vacuum. During this process, some physical phenomena such as baryogenesis, GW generation, and primordial black hole formation will happen. It can be expected that the velocity of the bubble wall has an impact on the final signal. For the GW power spectrum, numerical simulations indicate that faster bubble wall velocity enhances the signal intensity [102].

The velocity of the bubble wall in the plasma is governed by hydrodynamics and particle interactions. The way bubbles expand is divided into deflagration, detonation, hybrid and runaway cases [103], which influence the GW spectra through bubble collisions and interactions with the hydrodynamics. In order to understand the details of FOPT more accurately, many methods have been used to calculate the bubble wall velocity. As in Refs. [104–107], the local equilibrium hydrodynamic equations are applied to obtain the velocity. More generally, considering the effect of out of equilibrium, people need to solve the distribution function by the Boltzmann equation, which allows to obtain the velocity containing the backreaction [108–115]. In addition, the holographic method is also applied to the calculation of bubble wall velocity. In Refs. [63–65, 69, 70, 72], applying the gauge/gravity duality, the bubble velocity is calculated for strongly coupled hydrodynamics.

In this letter, the probe approximation is considered, i.e., we only account for the obstruction from the plasma fluid without the backaction. To investigate the real-time evolution, we transform the framework to the ingoing Eddington-Finkelstein coordinate, then the metric becomes

$$ds^2 = \frac{1}{z^2}[-f(z)dt^2 - 2dtdz + dr^2 + r^2d\theta^2 + r^2\sin^2\theta d\varphi^2]. \quad (14)$$

Under the coordinate transformation, the scalar field  $\chi$  is invariant, and its equation of motion becomes as follows

$$\partial_r^2 \chi(t, z, r) + \frac{2\partial_r \chi(t, z, r)}{r} + f(z)\partial_z^2 \chi(t, z, r) + \left(f'(z) - f(z)\Phi'(z) - \frac{3f(z)}{z}\right)\partial_z \chi(t, z, r) - \frac{\partial_\chi V(\chi)}{z^2} + \left(\frac{3}{z} + \Phi'(z)\right)\partial_t \chi(t, z, r) - 2\partial_t \partial_z \chi(t, z, r) = 0. \quad (15)$$

In order to solve Eq. (15), the equation requires suitable boundary conditions and initial condition. We choose the following boundary conditions at the center and edge

$$\partial_t \partial_r \chi|_{r=0} = \partial_t \partial_r \chi|_{r=R} = 0. \quad (16)$$

This means that the smoothness of the bubbles is ensured at the center and the edge. Of course, it is also possible to choose  $\partial_t \chi|_{r=R} = 0$  at the edge, i. e., a false vacuum at the far distance all the time. We find that there is almost no difference between the two choices when the radial dimensions are large enough. It can be foreseen that the choice of this paper is more reasonable when the space contains more than one bubble. At the conformal boundary, we have

$$\partial_t \partial_z \chi|_{z=0} = 0. \quad (17)$$

This corresponds to the fact that the current mass is fixed and its does not vary with time.

For the initial condition, we consider adding a perturbation  $\delta\chi$  to the bounce solution of the scalar field  $\chi_b$ . Because the meaning of the bounce solution is the critical bubble solution, i.e., any bubble larger than it will expand, and

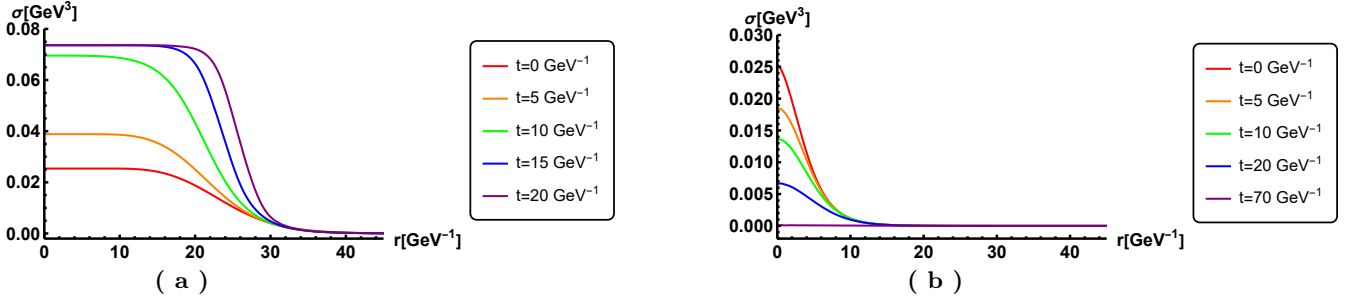


Figure 3. The panels (a) and (b) show the profiles of the bubbles at different times with  $T = 160$  MeV when positive and negative perturbations are added, respectively.

smaller than it will shrink. Since the bounce solution  $\chi_b$  does not vary with time, the selection of the perturbation is important, which will determine whether the bubble expands or shrinks. Therefore, the perturbation  $\delta\chi$  is not completely random, but is controlled to be positive or negative. In this paper, we choose the perturbation as follows

$$\delta\chi(z, r) = \mathcal{A}\chi_t(z)\{\exp[(r - r_0)^2] + 1\}^{-1}, \quad (18)$$

where  $\mathcal{A}$  is a constant that is small enough,  $\chi_t$  is the true vacuum solution at that temperature, and  $r_0$  is an arbitrary number.

The panels (a) and (b) of Fig. 3 show the evolution of the bubble with time at  $T = 160$  MeV when positive and negative perturbations are added, respectively. As seen in panel (a), when positive perturbation is added, the bubble goes through two steps. First the condensation value at the center of the bubble keeps growing until the true vacuum. After that, the structure of the bubble wall stabilizes and gradually expands outward. At times less than about  $t \simeq 15\text{GeV}^{-1}$ , the bubble is still in the first step, and when the time is greater than  $15\text{GeV}^{-1}$  the bubble enters the second step. If the temperature is  $170\text{MeV} \lesssim T \lesssim 174\text{MeV}$ , then the first step of bubble expansion does not occur. Of course, the exact timing of the distinction between the two steps is related to the amplitude of the perturbation, which is roughly equal in magnitude when the perturbation is small enough. The panel (b) displays the bubble shrinking with negative perturbation. As can be seen in the panel, the condensation value at the center of the bubble gradually decreases until the system completely returns to the false vacuum at  $t \simeq 70\text{GeV}^{-1}$ . The time of the bubble shrinking process is roughly comparable to the time of the first step of expansion, for bubbles that are neither too large nor too small.

To obtain the bubble wall velocity, we used the function  $\sigma(r) = \frac{\sigma_0(t)}{2}[-\tanh(\frac{r(t)-r_w(t)}{l_w(t)}) + 1]$  to fit the profile of the condensation. Here,  $\sigma_0$  is the condensation value at the center,  $r_w$  denotes the radius of the bubble, and  $l_w$  represents the thickness of the bubble wall. Fig. 4 shows the numerical and fitting results. It can be seen that the function fits the numerical results quite well except at the edges of the bubble walls. Therefore, we can define the velocity of the bubble wall by  $v(t) = dr_w(t)/dt$ . The panel (a) of Fig. 5 exhibits the bubble wall velocity as a function of time at a temperature of 160 MeV. It can be seen that the velocity gradually increases with time, while the acceleration gradually decreases. The velocity reaches its final velocity about  $0.31c$  when the time reaches about  $t \simeq 200\text{GeV}^{-1}$ . As for the relaxation time for the bubble to reach its final velocity, it depends on the strength of the perturbation. Numerical calculations show that the relaxation times with different perturbations are roughly equivalent. Note that the velocity is not well defined at time  $t \lesssim 20\text{GeV}^{-1}$ . This is because the bubble is still in the first step during this time and the wall configuration is changing and therefore not shown in the panel.

The final velocity of the bubble wall  $v_w$  is defined as  $v_w = \lim_{t \rightarrow \infty} v(t)$ . The panel (b) of Fig. 5 shows the final velocity of the bubble wall as a function of the pressure difference  $\Delta P$  between the inside and outside or the temperature  $T$ . According to the holographic principle, the pressure can be obtained from the free energy  $F = -P$ , as in Refs. [80, 81]. At low temperatures, the final velocity is approximately linear with respect to the pressure difference, while at temperatures close to the critical temperature, their relation exhibits nonlinear behavior. In Ref. [72], the relation between velocity and pressure difference has a nonlinear behavior. Although, the method used in Ref. [72] is different from the one used in this paper, the behavior exhibited is very similar. It can be seen from the panel that even if the temperature drops to 154 MeV, the final velocity still does not exceed sound speed  $c_s = 1/\sqrt{3}$  of the plasma, which corresponds to the deflagration case. This is in agreement with the results of Refs. [63, 64, 69, 72]. It is reasonable to speculate that in the bottom-up holographic model, the final velocity is always limited to the deflagrations region because the system contains a holographic dissipation mechanism [116]. While in Ref. [65], the Dp brane system can achieve bubble wall velocities close to the speed of light. Whether detonation and hybrid cases can be implemented in the bottom-up holographic model is still an open question.

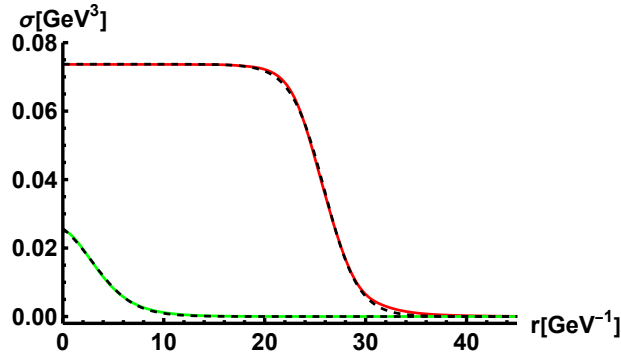


Figure 4. The condensate as a function of radial  $r$ , where the solid line is the numerical solution and the dashed line represents the fitting results of the hyperbolic tangent function.

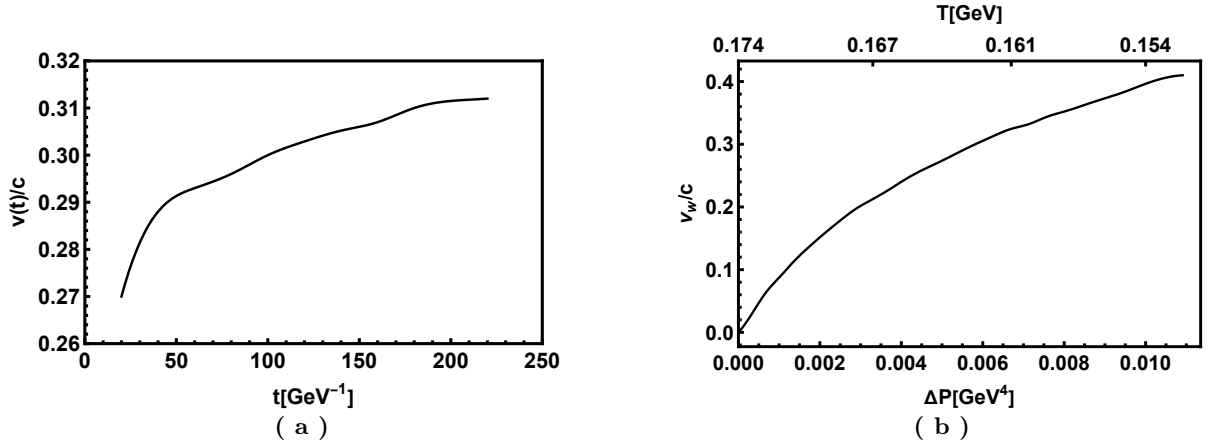


Figure 5. The panel (a) shows the bubble wall velocity as a function of time. The panel (b) shows the final velocity of the bubble wall as a function of the pressure difference  $\Delta P$  between the inside and outside or the temperature  $T$ .

#### IV. BUBBLES AND THIN WALL APPROXIMATION

In the previous section, we have obtained the bounce solution. By analyzing the properties of the holographic bounce solution, the characteristics of the strong FOPT can be understood qualitatively, which helps to understand its GW power spectrum. We know that there are three important characteristic temperatures during the dynamical FOPT that exhibit the details of the phase transition and are finally reflected in the GW. The first one is the critical temperature  $T_c$  of the phase transition, i.e., the temperature at which the free energy has a degenerate minimum. The rest are the nucleation temperature  $T_n$  and percolation temperature  $T_p$ , which represent the temperature of beginning nucleation and ending of phase transition, respectively. The temperature  $T_n$  and  $T_p$  are mainly determined by the profile of the Euclidean action  $\frac{S_b}{T}$  of bounce solution with temperature. In addition, the bubble wall thickness and bubble radius can be obtained from the bounce solution. In this section, we analyze the holographic behavior of the bounce solution with temperature. It should be noted that we only show the QCDPT with  $v_3 \neq 0$  (Model I). For  $v_6 \neq 0$  (Model II) or EWPT, the numerical results change slightly and the conclusions in the following still apply.

From Eq. (13) we can calculate the Euclidean action  $\frac{S_b}{T}$ . Fig. 6 shows the on-shell action  $\frac{S_b}{T}$  as a function of  $\frac{T}{T_c}$  calculated by the bounce solution. It can be seen from the figure that the value of the action decreases rapidly as the temperature decreases, and at about  $\frac{T}{T_c} \sim 0.99$ , i.e., at a temperature of about 172 MeV,  $\frac{S_b}{T}$  drops to 30. The nucleation temperature  $T_n$  can be given by relation  $\frac{S_b(T_n)}{T_n} \sim 180$  for QCDPT ( $\frac{S_b(T_n)}{T_n} \sim 140$  for EWPT) (a more rigorous definition is shown in the next section). Therefore, the nucleation temperature is very close to the critical temperature  $T_c \simeq T_n$ . Furthermore, at low temperatures, the action does not have a local minimum. Also, since the nucleation probability  $\Gamma$  is proportional to the action, it can be seen that bubbles are created rapidly and abundantly as the temperature decreases. Consequently, it is reasonable to suppose that the percolation temperature is close to the nucleation temperature  $T_n \simeq T_p$ . As shown above, the three characteristic temperatures have relation

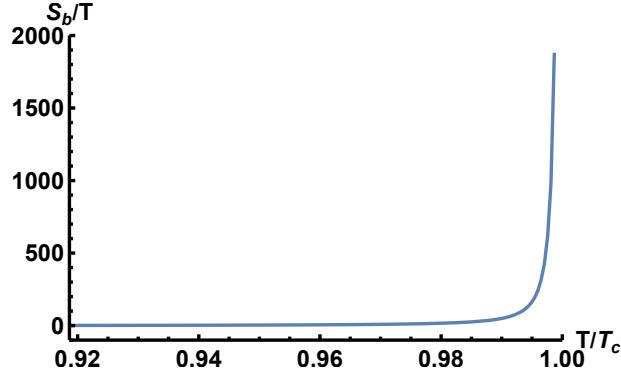


Figure 6. The Euclidean action  $\frac{S_b}{T}$  as a function of temperature.

$T_c \simeq T_n \simeq T_p$ , which corresponds to the supercooling case [117].

As in the previous section, we use hyperbolic tangent function interpolation condensation as a function of the radial  $r$ , shown following

$$\sigma(T, r) = \frac{\sigma_0(T)}{2} \left[ -\tanh\left(\frac{r - R_w(T)}{L_w(T)}\right) + 1 \right], \quad (19)$$

where  $\sigma_0$  is the condensation value at the center,  $R_w$  denotes the radius of the bubble, and  $L_w$  represents the thickness of the bubble wall. Unlike the previous section, these quantities are independent of time since the critical bubbles do not evolve with time. Fig. 7 displays the condensation  $\sigma_0$ , radius  $R_w$ , and thickness  $L_w$  as functions of temperature. As seen in panel (a), the condensation at the center increases with increasing temperature at  $T \lesssim 0.975T_c \sim 170\text{MeV}$  and has the opposite behavior at  $T \gtrsim 0.975T_c$ . Two factors with opposite effects influence this behavior. As can be seen in Fig. 1, the condensation value decreases continuously with increasing temperature; in contrast, as in Fig. 2, the critical bubble is larger at higher temperatures, which favors the generation of a true vacuum at the center. For the bubble radius  $R_w$ , panel (b) shows that the critical radius varies slightly at temperature  $T \lesssim 0.98T_c \sim 171\text{MeV}$ . However, at temperature  $T \gtrsim 0.98T_c$ , the critical radius of the bubble increases rapidly, which is not favorable for bubble generation. In contrast to the behavior of the bubble radius, the bubble wall thickness essentially does not vary with temperature. And the thickness changes slightly at low temperature  $T \lesssim 0.94T_c \sim 164\text{MeV}$ . This is because the hyperbolic function fitting is not a good choice at this time.

### A. Thin-wall approximation

From the previous discussion, it is clear that in this holographic model, the FOPT is supercooled. As in Ref. [117], the thin-wall approximation can be applied in this case. Under this approximation, many physical quantities, such as latent heat, duration time of phase transition and surface tension of bubble, have simpler forms and can be obtained more easily. In this section, we estimate the surface tension and the parameters  $\alpha$  and  $\beta/H$  using the Euclidean action obtained previously. Among them, the parameters  $\alpha$  and  $\beta/H$  are very important for the GW power spectrum.

From Ref. [117], the parameter  $\alpha$  is

$$\alpha \simeq \frac{15}{2\pi^2} \frac{L_c}{g_*(T_c)T_c^4}, \quad (20)$$

where  $g_*$  is the relativistic degree of freedom of the system and  $L_c$  is the latent heat of phase transition. For QCDPT (EWPT), the degrees of freedom can be approximated as  $g_* \simeq 10$  ( $g_* \simeq 100$ ). Under the thin-wall approximation, the latent heat has the following form

$$L_c = -T \left. \frac{\partial \Delta V_{\text{eff}}(\langle \phi \rangle_T, T)}{\partial T} \right|_{T=T_c} = T \left. \frac{\partial \Delta F(\langle \phi \rangle_T, T)}{\partial T} \right|_{T=T_c}, \quad (21)$$

with difference of the free energy  $\Delta F$ . The calculation of the free energy  $F$  can be found in Refs. [80, 81]. Within the approximation, the three-dimensional Euclidean action  $S_b$  can be divided into two parts, as follows

$$S_b(T) = -\frac{4\pi}{3} R_w(T) \varepsilon(T) + 4\pi R_w(T)^2 \sigma_w(T), \quad (22)$$



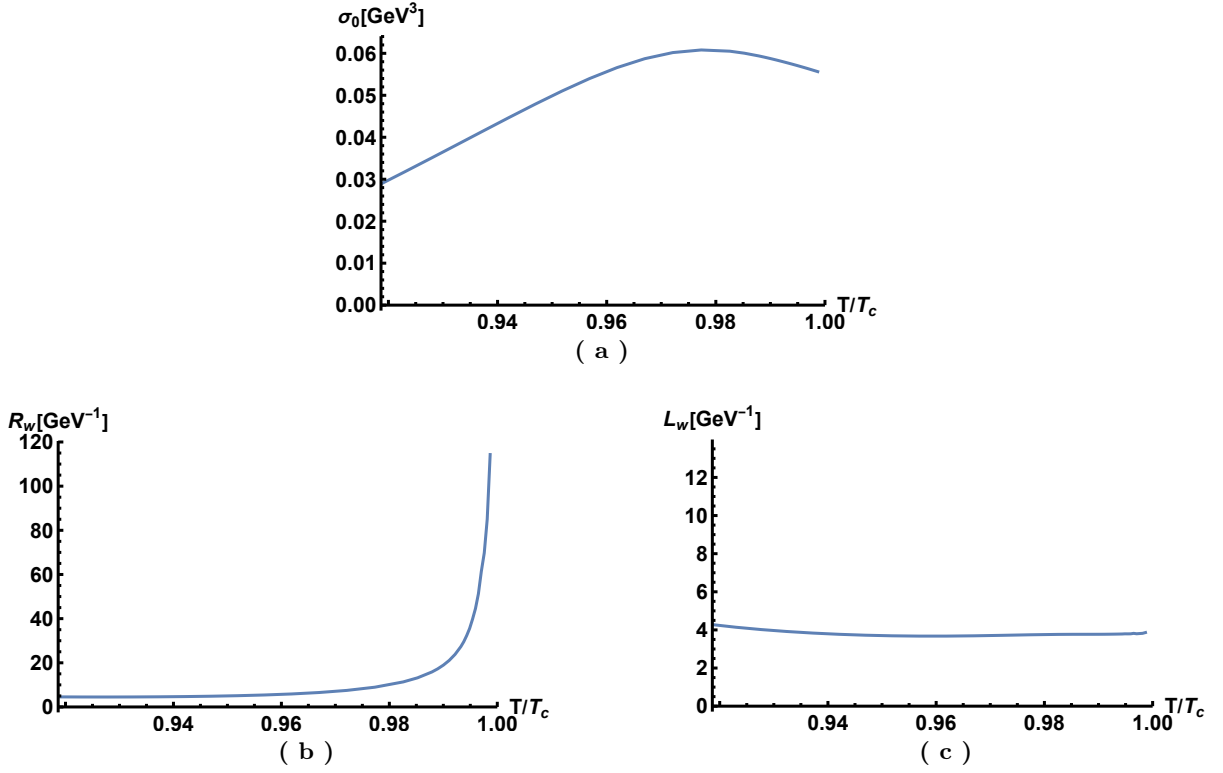


Figure 7. The panels (a), (b) and (c) show the condensation value at the center  $\sigma_0$ , the bubble radius  $R_w$  and the bubble wall thickness  $L_w$  as functions of the temperature, respectively.

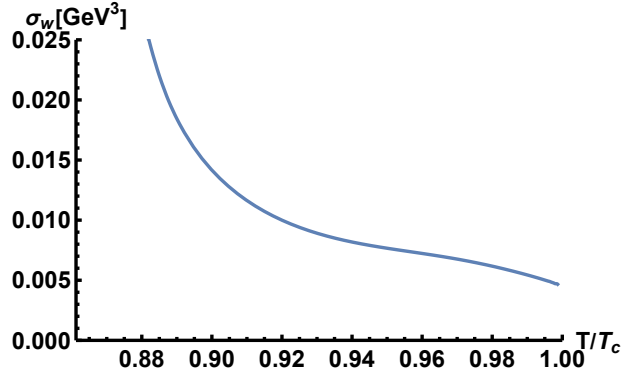


Figure 8. The surface tension  $\sigma_w$  of the bubble wall as a function of temperature.

with the  $\varepsilon(T) = \Delta V_{\text{eff}}(\langle\phi\rangle_T, T)$  and surface tension  $\sigma_w$  of the bubble wall. From the above equation, it can be seen that the energy of the critical bubble consists of the vacuum energy inside the bubble and the surface energy of the bubble wall. With the bubble radius previously calculated, the surface tension can be obtained as shown in Fig. 8. For the low-temperature region in the figure, the result is not reliable because the thin-wall approximation no longer applies.

Also from Ref. [117], the inverse of duration time  $\beta/H$  of the phase transition is given as

$$\frac{\beta}{H} = \left( \frac{3}{4\pi} \frac{T_c L_c^2}{\sigma_w(T_c)^3} \right)^{1/2} \left( \frac{S_b(T_p)}{T_p} \right)^{3/2}, \quad (23)$$

with the percolation temperature  $T_p$ . With the above definitions and the relation  $T_c \simeq T_n \simeq T_p$ , the final results of parameters  $\alpha$  and  $\beta/H$  are shown in Tab. I. Here, the velocity  $v_w$  is calculated at the percolation temperature  $T_p$ . From the table, we can find that for QCDPT, the parameter  $\alpha$  is greater than 1, about 4-5, which is strongly FOPT case, and the parameter  $\beta/H$  is large, which means that the phase transition ends rapidly. For EWPT, the strength

Thin-wall approx	QCDPT	EWPT
$\alpha$	4-6	0.4-0.6
$\beta/H$	30000-60000	6000-20000
$v_w$	0.04	0.1

Table I. The parameters  $\alpha$ ,  $\beta/H$  and the bubble wall velocity  $v_w$  estimated by the thin-wall approximation during QCDPT and EWPT.

parameter  $\alpha$  is less than 1, while the inverse of the duration time remains large, which means that the phase transition is sufficiently fast, that is, the so-called weakly supercooled FOPT.

## V. STOCHASTIC GRAVITATIONAL WAVES

When the system reaches the nucleation temperature, bubbles will be created, and they will collide and merge together in the plasma. Then the false vacuum will be transformed into the true vacuum. In this process, part of the system's energy is eventually converted into GW radiation. Within the linear approximation, the total GW power spectra can be written as

$$h^2\Omega_{\text{GW}} \simeq h^2\Omega_{\text{coll}} + h^2\Omega_{\text{sw}} + h^2\Omega_{\text{turb}}, \quad (24)$$

where  $\Omega_{\text{coll}}$  comes from bubble collisions [103, 118–126],  $\Omega_{\text{sw}}$  from acoustic waves in the plasma after the collision [127–131], and  $\Omega_{\text{turb}}$  from magnetohydrodynamic turbulence in the plasma [132–139].

In the previous section we have found that for the holographic model, the final velocity of the bubble wall is less than the speed of sound, i.e., the non-runaway case. According to Refs. [102, 103, 121, 140–142], the GWs generated by collisions in the non-runaway case can be neglected with respect to acoustic waves and magnetohydrodynamic turbulence. Therefore, the total power spectrum is approximated to

$$h^2\Omega_{\text{GW}} \simeq h^2\Omega_{\text{sw}} + h^2\Omega_{\text{turb}}. \quad (25)$$

From numerical simulations [130], the power spectrum from sound waves has the form of

$$h^2\Omega_{\text{sw}}(f) = 2.65 \times 10^{-6} \left( \frac{H}{\beta} \right) \left( \frac{\kappa_v \alpha}{1 + \alpha} \right)^2 \left( \frac{100}{g_*} \right)^{\frac{1}{3}} v_w S_{\text{sw}}(f), \quad (26)$$

$$S_{\text{sw}}(f) = (f/f_{\text{sw}})^3 \left( \frac{7}{4 + 3(f/f_{\text{sw}})^2} \right)^{7/2}, \quad (27)$$

$$f_{\text{sw}} = 1.9 \times 10^{-2} \text{mHz} \frac{1}{v_w} \left( \frac{\beta}{H} \right) \left( \frac{T_p}{100 \text{GeV}} \right) \left( \frac{g_*}{100} \right)^{\frac{1}{6}}, \quad (28)$$

where the factor  $\kappa_v$  represents the ratio of vacuum energy transformed into bulk motion. The specific form of the factor  $\kappa_v$  depends on the bubble wall velocity and has the following form in the limits of large and small velocities

$$\kappa_v \simeq \begin{cases} \alpha (0.73 + 0.083\sqrt{\alpha} + \alpha)^{-1}, & v_w \sim 1, \\ v_w^{6/5} 6.9\alpha (1.36 - 0.037\sqrt{\alpha} + \alpha)^{-1}, & v_w \lesssim 0.1. \end{cases} \quad (29)$$

From the Tab. I, it is obtained that the velocity is about  $v_w \sim 0.1$ , since the phase transition of the holographic model is supercooled. Therefore, in this paper, the expression for the factor  $\kappa_v$  is

$$\kappa_v = v_w^{6/5} 6.9\alpha (1.36 - 0.037\sqrt{\alpha} + \alpha)^{-1}. \quad (30)$$

For the power spectrum from the Kolmogorov-type turbulence, numerical simulations show that it can be given as [132, 138, 143]

$$h^2\Omega_{\text{turb}}(f) = 3.35 \times 10^{-4} \left( \frac{H}{\beta} \right) \left( \frac{\kappa_{\text{turb}} \alpha}{1 + \alpha} \right)^{\frac{3}{2}} \left( \frac{100}{g_*} \right)^{1/3} v_w S_{\text{turb}}(f), \quad (31)$$

$$S_{\text{turb}}(f) = \frac{(f/f_{\text{turb}})^3}{[1 + (f/f_{\text{turb}})]^{\frac{11}{3}} (1 + 8\pi f/h_*)}, \quad (32)$$

$$f_{\text{turb}} = 2.7 \times 10^{-2} \text{mHz} \frac{1}{v_w} \left( \frac{\beta}{H} \right) \left( \frac{T_p}{100 \text{GeV}} \right) \left( \frac{g_*}{100} \right)^{\frac{1}{6}}, \quad (33)$$

where the Hubble rate  $h_*$  is

$$h_* = 16.5 \times 10^{-3} \text{mHz} \left( \frac{T_p}{100 \text{GeV}} \right) \left( \frac{g_*}{100} \right)^{\frac{1}{6}}. \quad (34)$$

In this paper, referring to the numerical results of the Refs. [102, 130], the factor  $\kappa_{\text{turb}}$  is chosen to be

$$\kappa_{\text{turb}} = 0.05 \kappa_v. \quad (35)$$

It should be noted that, due to the complexity of turbulence, more research is still needed on the exact form of the factor  $\kappa_{\text{turb}}$  and its relation to  $\kappa_v$ . In this holographic model, the choice can be reasonable considering that the phase transition may end rapidly and therefore the effect of turbulence is expected to be suppressed.

In the GW power spectrum, the parameters  $\alpha$  and  $\beta/H$  are important, which represent the vacuum energy release and duration time of the phase transition, respectively. The parameter  $\alpha$  is defined as

$$\alpha \equiv \frac{1}{\rho_{\text{rad}}} \left( \Delta V_{\text{eff}} - \frac{T}{4} \frac{\partial \Delta V_{\text{eff}}}{\partial T} \right) \Big|_{T=T_p} = -\frac{1}{\rho_{\text{rad}}} \left( \Delta F - \frac{T}{4} \frac{\partial \Delta F}{\partial T} \right) \Big|_{T=T_p}, \quad (36)$$

with radiation energy density

$$\rho_{\text{rad}} = g_* \frac{\pi^2}{30} T^4. \quad (37)$$

The inverse of the duration time is defined as

$$\frac{\beta}{H} \equiv T \frac{d}{dT} \left( \frac{S_b}{T} \right) \Big|_{T=T_p}. \quad (38)$$

The definitions of the other two characteristic temperatures of the phase transition, i. e., nucleation temperature  $T_n$  and percolation temperature  $T_p$ , are shown below. The nucleation temperature is defined as one bubble per unit Hubble volume and is written as

$$N(T_n) = \int_{T_n}^{T_c} \frac{dT}{T} \frac{\Gamma(T)}{H(T)^4} = 1, \quad (39)$$

where the nucleation rate  $\Gamma(T)$  is given in Eq. (12) and the Hubble parameter  $H(T)$  is

$$H(T) = \sqrt{\frac{\rho_{\text{rad}} + \rho_{\text{vac}}}{3M_{\text{pl}}^2}}, \quad (40)$$

with reduced Planck mass  $M_{\text{pl}} = 2.435 \cdot 10^{18}$  GeV. Referring to Refs. [144–146], the probability of a false vacuum is defined as

$$P(T) = e^{-I(T)}, \quad (41)$$

with

$$I(T) = \frac{4\pi}{3} \int_T^{T_c} dT' \frac{\Gamma(T')}{H(T')^4} \left( \int_T^{T'} dT'' \frac{v_w(T'')}{H(T'')} \right)^3. \quad (42)$$

The percolation temperature is defined as  $I(T_p) \simeq 0.34$ , which is the temperature when the probability of false vacuum is about  $P(T_p) \simeq 0.7$ .

The Tab. II shows the quantities related to the phase transition in different holographic models. Here, the velocity  $v_w$  is selected at the percolation temperature  $T_p$ . Compare to Table I, we can see that the rigorous results are very close to that of thin-wall approximation. This further verifies the reliability of the approximation in the holographic model. It should be noted that the strength parameter  $\alpha$  of QCDPT is greater than 1, which would be a strongly supercooled FOPT. For EWPT, FOPT is weakly supercooled. It is worth noting that although QCDPT is strongly supercooled, its properties are very similar to those of the EWPT and there are no minimum values of the weights  $S_b/T$  as mentioned in the Ref. [117]. Furthermore, for parameters  $\alpha$  and  $\beta/H$ , we find an inverse relation between them, which is similar to that of Ref. [117]. For Models I and II, we found that Model II ( $v_6 \neq 0$ ) has lower percolation temperature and larger bubble wall velocity, which favors a bigger GW signal.

	QCDPT		EWPT	
Model	I ( $v_3 \neq 0$ )	II ( $v_6 \neq 0$ )	I ( $v_3 \neq 0$ )	II ( $v_6 \neq 0$ )
$g_*$	10		100	
$\alpha$	4.881	6.142	0.238	0.763
$\beta/H$	41151	23276	17198	7238
$v_w$	0.027	0.041	0.063	0.125
$T_c[\text{GeV}]$	0.1741		122.1	
$T_n[\text{GeV}]$	0.1733	0.1712	120.7	118.1
$T_p[\text{GeV}]$	0.1732	0.1703	120.4	117.6

Table II. The critical temperature  $T_c$ , nucleation temperature  $T_n$ , percolation temperature  $T_p$  of phase transition, parameters  $\alpha$ ,  $\beta/H$ , and bubble wall velocity  $v_w$  in different holographic models.

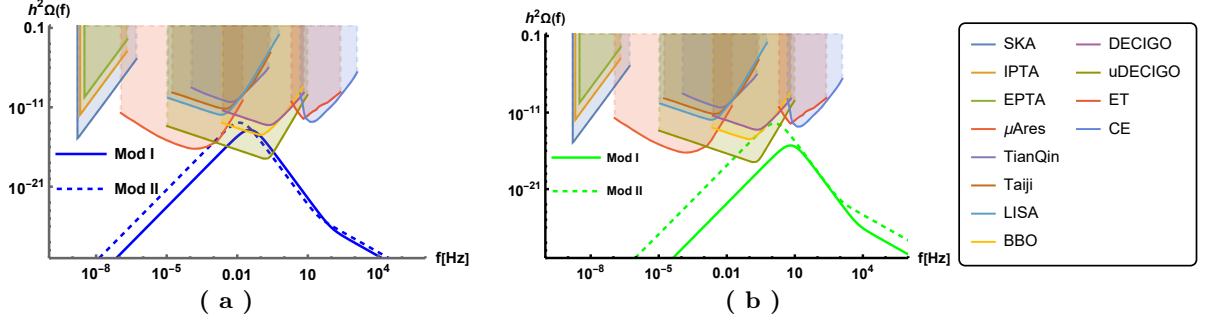


Figure 9. The GW power spectra in different holographic models, where the blue (a) and green (b) lines represent QCDPT and EWPT, respectively.

From Tab. II, we also find that the results of the holographic model differ significantly from those of the traditional calculations in quantum field theory. In quantum field theory, the parameter  $\alpha$  is generally not larger than 0.01 and the latent heat released in the phase transition is not large. However, the strength of the phase transition is greater than 0.1 for both color brane [54] and flavor brane in the holographic model. For the parameter  $\beta/H$ , field theory calculations show that it is generally not larger than 1000. But for the holographic model, the parameter  $\beta/H$  is larger than 5000 during QCDPT or EWPT. This means that the duration time of the strongly coupled phase transition is shorter compared to the weakly coupled case. As for the bubble wall velocity, one would expect it to be close to the speed of light  $c$ . Unfortunately, the holographic results suggest that the bubble wall velocity is smaller than the sound speed of the plasma.

The GW power spectra of QCDPT and EWPT for different holographic models are exhibited in Fig. 9. Due to the large value of  $\beta/H$ , the peak frequency of GW is larger compared to the results of quantum field theory, causing a right shift in the sensitive frequency interval of GW. For the holographic model of QCDPT, the peak frequency is about 0.01 Hz. In addition, since the bubble wall velocity  $v_w$  is much less than the speed of light  $c$ , the GW signal  $h^2\Omega$  can only reach about  $10^{-13} - 10^{-14}$ , which can be detected by  $\mu\text{Ares}$ , BBO and Ultimate-DECIGO for Model II, and by BBO and Ultimate-DECIGO for Model I. For EWPT, the peak frequency is around 1 – 10 Hz, when the GW spectrum  $h^2\Omega$  reaches about  $10^{-12} - 10^{-16}$ . For Model I, the GW can be detected by BBO and Ultimate-DECIGO, but for Model II, it is not detectable by future experiments.

## VI. CONCLUSION AND DISCUSSION

In this paper, holographic bounce solutions, bubble wall velocities and GW power spectra are studied and discussed in holographic QCD and EW models. For holographic models with first-order phase transitions, holographic bounce solutions can be obtained by setting appropriate boundary conditions. By adding positive and negative perturbations to the bounce solution, the bubble expands or shrinks and the final velocity of the bubble wall can be given. It turns out that the final velocity is still smaller than the speed of sound in the plasma, i. e. the deflagration case, even if the phase transition temperature is very low. Moreover, we find that the critical temperature  $T_c$ , nucleation temperature  $T_n$  and percolation temperature  $T_p$  of the phase transition are close to each other, which makes the holographic bubble fit well with the results of thin-wall approximation. Furthermore, the strength parameter  $\alpha$  calculated by the

holographic model is about  $\alpha \sim 5$  for QCDPT ( $\alpha \sim 0.5$  for EWPT) and the inverse of the duration time  $\beta/H$  is about  $\beta/H \sim 10000$ , and they are quite different from the weakly coupled field theory results. For QCDPT, the GW power spectrum can reach  $10^{-13} - 10^{-14}$  around the peak frequency 0.01 Hz, which can be detected by  $\mu$ Ares, BBO and Ultimate-DECIGO for  $v_6 \neq 0$  (Model II), and by BBO and Ultimate-DECIGO for  $v_3 \neq 0$  (Model I). For EWPT, the GW power spectrum can reach  $10^{-12} - 10^{-16}$  around the peak frequency 1 – 10 Hz, which can be detected by BBO and Ultimate-DECIGO for  $v_6 \neq 0$  (Model II), but not by future experiments for  $v_3 \neq 0$  (Model I).

Referring to the quantum bounce solutions proposed by Coleman and Callan[92, 93] with Neumann boundary condition at the center and Dirichlet boundary condition at the edge, the holographic bounce solution can be yielded. We found that the radius of the critical bubble and the value of condensation at the center reduced with decreasing temperature. If a small positive or negative perturbation is added to the holographic bounce solution, the bubble starts to expand or shrink. Through a long enough evolution, the velocity of the bubble wall reaches a constant value. It turns out that in this holographic model, the bubble velocity is deflagration, i.e., it is less than the speed of sound of the system. Although our calculations are under the probe approximation, that is, without a push to the fluid, the conclusions are similar to the Refs. [63–65, 69, 70, 72]. How to get detonation and hybrid cases in the bottom-up model remains an open question.

The radius of the critical bubble and the thickness of the bubble wall can be obtained by the Euclidean action. We found that the bubble radius drops rapidly with decreasing temperature while the wall thickness varies little with temperature. In addition, we find that the critical temperature, nucleation temperature and percolation temperature are close to each other during the holographic phase transition. Therefore the thin-wall approximation is considered to estimate the strength and duration time of the phase transition. It turns out that the more rigorous calculations agree well with the approximation results, verifying the reliability of the approximation.

With the holographic bounce solution and the bubble final velocity, we calculated the GW power spectra of QCDPT and EWPT. We find that the strength parameter  $\alpha$  and the inverse of the duration time  $\beta/H$  calculated by the holographic model differ significantly from the weakly coupled field theory results, which impact the GW signal. The parameter  $\alpha$  can reach about 5 for QCDPT, which is strong phase transition, and about 0.5 for EWPT. The parameter  $\beta/H$  is about 30,000 for QCDPT and about 10,000 for EWPT, so the holographic phase transition is sufficiently fast. Due to the large parameter  $\beta/H$ , the peak frequency shifts rightward compared to the field theory results. In addition, the GW spectrum is suppressed due to the small bubble expansion speed. Eventually, for QCDPT, it can be detected by  $\mu$ Ares, BBO and Ultimate-DECIGO for Model II and by BBO and Ultimate-DECIGO for Model I. For EWPT, Model II is detectable, while Model I cannot be detected by future experiments. Whether it is QCDPT or EWPT, the FOPT caused by the sextic term has a larger  $\alpha$  and smaller  $\beta/H$  and higher GW energy than that caused by the cubic term.

For primordial black holes, the formula of mechanism [147] cannot be applied because the speed of the bubble at the phase transition is much smaller than the speed of light  $c$ . Therefore, it cannot be determined whether the black holes have sufficient probability to be produced. However, since the small bubble wall velocity may lead to a small energy density perturbation during the collision, we can speculate that the primordial black hole is difficult to produce in this holographic model. Also, as in Ref. [148], the large parameter  $\beta/H$  is not favorable for the formation of primordial black holes.

## ACKNOWLEDGMENTS

We thank Anping Huang, Mingqiu Li, Jingdong Shao, Dianwei Wang, and Qi-Shu Yan for helpful discussions. This work is supported by the China Postdoctoral Science Foundation under Grant No. 2021M703169, the Fundamental Research Funds for the Central Universities E2E46303X2, the National Natural Science Foundation of China (NSFC) Grant Nos:12235016, 12221005, 11725523, 11735007, 12275108, and the Strategic Priority Research Program of Chinese Academy of Sciences under Grant Nos XDB34030000 and XDPB15, the start-up funding from University of Chinese Academy of Sciences(UCAS), the Fundamental Research Funds for the Central Universities, and the Guangdong Pearl River Talents Plan under Grant No. 2017GC010480.

- 
- [1] A. Einstein, Sitzungsber. Preuss. Akad. Wiss. Berlin (Math. Phys.) **1916**, 1 (1916).
  - [2] A. Einstein, Sitzungsber. Preuss. Akad. Wiss. Berlin (Math. Phys.) p. 154 (1918).
  - [3] R. A. Hulse and J. H. Taylor, Astrophys. J. Lett. **195**, L51 (1975).
  - [4] B. P. Abbott et al. (LIGO Scientific, Virgo), Phys. Rev. Lett. **116**, 061102 (2016), 1602.03837.
  - [5] R. Abbott et al. (LIGO Scientific, VIRGO, KAGRA) (2021), 2111.03606.
  - [6] Z. Arzoumanian et al. (NANOGrav), Astrophys. J. Lett. **905**, L34 (2020), 2009.04496.

- [7] M. Maggiore, *Gravitational Waves. Vol. 1: Theory and Experiments*, Oxford Master Series in Physics (Oxford University Press, 2007), ISBN 978-0-19-857074-5, 978-0-19-852074-0.
- [8] R.-G. Cai, Z. Cao, Z.-K. Guo, S.-J. Wang, and T. Yang, *Natl. Sci. Rev.* **4**, 687 (2017), 1703.00187.
- [9] M. Maggiore, *Gravitational Waves. Vol. 2: Astrophysics and Cosmology* (Oxford University Press, 2018), ISBN 978-0-19-857089-9.
- [10] N. Christensen, *Rept. Prog. Phys.* **82**, 016903 (2019), 1811.08797.
- [11] M. Bailes et al., *Nature Rev. Phys.* **3**, 344 (2021).
- [12] J. Aasi et al. (LIGO Scientific), *Class. Quant. Grav.* **32**, 074001 (2015), 1411.4547.
- [13] F. Acernese et al. (VIRGO), *Class. Quant. Grav.* **32**, 024001 (2015), 1408.3978.
- [14] M. Punturo et al., *Class. Quant. Grav.* **27**, 194002 (2010).
- [15] B. P. Abbott et al. (LIGO Scientific), *Class. Quant. Grav.* **34**, 044001 (2017), 1607.08697.
- [16] P. Amaro-Seoane et al. (LISA) (2017), 1702.00786.
- [17] S. Kawamura et al., *Class. Quant. Grav.* **23**, S125 (2006).
- [18] H. Kudoh, A. Taruya, T. Hiramatsu, and Y. Himemoto, *Phys. Rev. D* **73**, 064006 (2006), gr-qc/0511145.
- [19] G. M. Harry, P. Fritschel, D. A. Shaddock, W. Folkner, and E. S. Phinney, *Class. Quant. Grav.* **23**, 4887 (2006), [Erratum: *Class. Quant. Grav.* **23**, 7361 (2006)].
- [20] W.-R. Hu and Y.-L. Wu, *Natl. Sci. Rev.* **4**, 685 (2017).
- [21] J. Luo et al. (TianQin), *Class. Quant. Grav.* **33**, 035010 (2016), 1512.02076.
- [22] R. N. Manchester et al., **30**, 17 (2013), 1210.6130.
- [23] M. Kramer and D. J. Champion, *Class. Quant. Grav.* **30**, 224009 (2013).
- [24] M. A. McLaughlin, *Class. Quant. Grav.* **30**, 224008 (2013), 1310.0758.
- [25] R. N. Manchester, *Class. Quant. Grav.* **30**, 224010 (2013), 1309.7392.
- [26] K. Kajantie, M. Laine, K. Rummukainen, and M. E. Shaposhnikov, *Phys. Rev. Lett.* **77**, 2887 (1996), hep-ph/9605288.
- [27] M. Gurtler, E.-M. Ilgenfritz, and A. Schiller, *Phys. Rev. D* **56**, 3888 (1997), hep-lat/9704013.
- [28] F. Csikor, Z. Fodor, and J. Heitger, *Phys. Rev. Lett.* **82**, 21 (1999), hep-ph/9809291.
- [29] Z. Fodor and S. D. Katz, *Phys. Lett. B* **534**, 87 (2002), hep-lat/0104001.
- [30] H.-T. Ding, F. Karsch, and S. Mukherjee, *Int. J. Mod. Phys. E* **24**, 1530007 (2015), 1504.05274.
- [31] J. M. Cline and P.-A. Lemieux, *Phys. Rev. D* **55**, 3873 (1997), hep-ph/9609240.
- [32] P. Basler, M. Krause, M. Muhlleitner, J. Wittbrodt, and A. Wlotzka, *JHEP* **02**, 121 (2017), 1612.04086.
- [33] G. C. Dorsch, S. J. Huber, T. Konstandin, and J. M. No, *JCAP* **05**, 052 (2017), 1611.05874.
- [34] M. Li, Q.-S. Yan, Y. Zhang, and Z. Zhao, *JHEP* **03**, 267 (2021), 2012.13686.
- [35] T. Appelquist, J. Terning, and L. C. R. Wijewardhana, *Phys. Rev. Lett.* **77**, 1214 (1996), hep-ph/9602385.
- [36] F. Sannino and J. Schechter, *Phys. Rev. D* **60**, 056004 (1999), hep-ph/9903359.
- [37] T. Appelquist, P. S. Rodrigues da Silva, and F. Sannino, *Phys. Rev. D* **60**, 116007 (1999), hep-ph/9906555.
- [38] J. M. Maldacena, *Adv. Theor. Math. Phys.* **2**, 231 (1998), hep-th/9711200.
- [39] S. S. Gubser, I. R. Klebanov, and A. M. Polyakov, *Phys. Lett. B* **428**, 105 (1998), hep-th/9802109.
- [40] E. Witten, *Adv. Theor. Math. Phys.* **2**, 253 (1998), hep-th/9802150.
- [41] J. Erdmenger, N. Evans, I. Kirsch, and E. Threlfall, *Eur. Phys. J. A* **35**, 81 (2008), 0711.4467.
- [42] T. Sakai and S. Sugimoto, *Prog. Theor. Phys.* **113**, 843 (2005), hep-th/0412141.
- [43] T. Sakai and S. Sugimoto, *Prog. Theor. Phys.* **114**, 1083 (2005), hep-th/0507073.
- [44] J. Erlich, E. Katz, D. T. Son, and M. A. Stephanov, *Phys. Rev. Lett.* **95**, 261602 (2005), hep-ph/0501128.
- [45] A. Karch, E. Katz, D. T. Son, and M. A. Stephanov, *Phys. Rev. D* **74**, 015005 (2006), hep-ph/0602229.
- [46] U. Gursoy and E. Kiritsis, *JHEP* **02**, 032 (2008), 0707.1324.
- [47] S. S. Gubser and A. Nellore, *Phys. Rev. D* **78**, 086007 (2008), 0804.0434.
- [48] J. Grefa, J. Noronha, J. Noronha-Hostler, I. Portillo, C. Ratti, and R. Rougemont, *Phys. Rev. D* **104**, 034002 (2021), 2102.12042.
- [49] D. Li and M. Huang, *JHEP* **11**, 088 (2013), 1303.6929.
- [50] Y. Chen, D. Li, and M. Huang, *Commun. Theor. Phys.* **74**, 097201 (2022), 2206.00917.
- [51] K. Haba, S. Matsuzaki, and K. Yamawaki, *Prog. Theor. Phys.* **120**, 691 (2008), 0804.3668.
- [52] S. Matsuzaki and K. Yamawaki, *Phys. Rev. D* **86**, 115004 (2012), 1209.2017.
- [53] D. Elander and M. Piai, *Nucl. Phys. B* **867**, 779 (2013), 1208.0546.
- [54] Y. Chen, M. Huang, and Q.-S. Yan, *JHEP* **05**, 178 (2018), 1712.03470.
- [55] K. Bitaghsir Fadafan, W. Clemens, and N. Evans, *Phys. Rev. D* **98**, 066015 (2018), 1807.04548.
- [56] Y. Chen, X.-J. Bi, and M. Huang, *Chin. Phys. C* **44**, 093102 (2020), 1912.11682.
- [57] R. Contino, Y. Nomura, and A. Pomarol, *Nucl. Phys. B* **671**, 148 (2003), hep-ph/0306259.
- [58] K. Agashe, R. Contino, and A. Pomarol, *Nucl. Phys. B* **719**, 165 (2005), hep-ph/0412089.
- [59] D. Croon, B. M. Dillon, S. J. Huber, and V. Sanz, *JHEP* **07**, 072 (2016), 1510.08482.
- [60] D. Espriu and A. Katanaeva (2017), 1706.02651.
- [61] M. Attems, Y. Bea, J. Casallerrey-Solana, D. Mateos, M. Triana, and M. Zilhão, *Phys. Rev. Lett.* **121**, 261601 (2018).
- [62] M. Attems, Y. Bea, J. Casallerrey-Solana, D. Mateos, and M. Zilhão, *JHEP* **01**, 106 (2020).
- [63] Y. Bea, J. Casallerrey-Solana, T. Giannakopoulos, D. Mateos, M. Sanchez-Garitaonandia, and M. Zilhão, *Phys. Rev. D* **104**, L121903 (2021).
- [64] Y. Bea, J. Casallerrey-Solana, T. Giannakopoulos, A. Jansen, S. Krippendorff, D. Mateos, M. Sanchez-Garitaonandia, and M. Zilhão (2021), 2112.15478.

- [65] F. Bigazzi, A. Caddeo, T. Canneti, and A. L. Cotrone, JHEP **08**, 090 (2021).
- [66] F. Bigazzi, A. Caddeo, A. L. Cotrone, and A. Paredes, JHEP **04**, 094 (2021).
- [67] F. R. Ares, O. Henriksson, M. Hindmarsh, C. Hoyos, and N. Jokela, Phys. Rev. D **105**, 066020 (2022).
- [68] F. R. Ares, O. Henriksson, M. Hindmarsh, C. Hoyos, and N. Jokela, Phys. Rev. Lett. **128**, 131101 (2022).
- [69] Y. Bea, J. Casalderrey-Solana, T. Giannakopoulos, A. Jansen, D. Mateos, M. Sanchez-Garitaonandia, and M. Zilhão, JHEP **09**, 008 (2022).
- [70] Y. Bea, J. Casalderrey-Solana, T. Giannakopoulos, D. Mateos, M. Sanchez-Garitaonandia, and M. Zilhão, JHEP **06**, 025 (2022).
- [71] Q. Chen, Y. Liu, Y. Tian, B. Wang, C.-Y. Zhang, and H. Zhang (2022), 2209.12789.
- [72] R. A. Janik, M. Jarvinen, H. Soltanpanahi, and J. Sonnenschein, Phys. Rev. Lett. **129**, 081601 (2022).
- [73] M. Ahmadvand and K. Bitaghsir Fadafan, Phys. Lett. B **772**, 747 (2017), 1703.02801.
- [74] M. Ahmadvand and K. Bitaghsir Fadafan, Phys. Lett. B **779**, 1 (2018), 1707.05068.
- [75] S. Rezapour, K. Bitaghsir Fadafan, and M. Ahmadvand, Annals Phys. **437**, 168731 (2022), 2006.04265.
- [76] Z.-R. Zhu, J. Chen, and D. Hou, Eur. Phys. J. A **58**, 104 (2022), 2109.09933.
- [77] O. O. Novikov and A. A. Shavrin (2022), 2209.02331.
- [78] R.-G. Cai, S. He, L. Li, and Y.-X. Wang (2022), 2201.02004.
- [79] S. He, L. Li, Z. Li, and S.-J. Wang (2022), 2210.14094.
- [80] K. Chelabi, Z. Fang, M. Huang, D. Li, and Y.-L. Wu, Phys. Rev. D **93**, 101901 (2016), 1511.02721.
- [81] K. Chelabi, Z. Fang, M. Huang, D. Li, and Y.-L. Wu, JHEP **04**, 036 (2016), 1512.06493.
- [82] X. Chen, D. Li, D. Hou, and M. Huang, JHEP **03**, 073 (2020), 1908.02000.
- [83] T. Appelquist and G. Triantaphyllou, Phys. Lett. B **278**, 345 (1992).
- [84] R. Sundrum and S. D. H. Hsu, Nucl. Phys. B **391**, 127 (1993), hep-ph/9206225.
- [85] T. Appelquist and F. Sannino, Phys. Rev. D **59**, 067702 (1999), hep-ph/9806409.
- [86] M. Harada, M. Kurachi, and K. Yamawaki, Prog. Theor. Phys. **115**, 765 (2006), hep-ph/0509193.
- [87] M. Kurachi and R. Shrock, Phys. Rev. D **74**, 056003 (2006), hep-ph/0607231.
- [88] M. Kurachi, R. Shrock, and K. Yamawaki, Phys. Rev. D **76**, 035003 (2007), 0704.3481.
- [89] A. Karch, E. Katz, D. T. Son, and M. A. Stephanov, JHEP **04**, 066 (2011).
- [90] R. Becker and W. Döring, Annalen der physik **416**, 719 (1935).
- [91] J. S. Langer, Annals Phys. **54**, 258 (1969).
- [92] S. R. Coleman, Phys. Rev. D **15**, 2929 (1977), [Erratum: Phys.Rev.D 16, 1248 (1977)].
- [93] C. G. Callan, Jr. and S. R. Coleman, Phys. Rev. D **16**, 1762 (1977).
- [94] I. Affleck, Phys. Rev. Lett. **46**, 388 (1981).
- [95] A. D. Linde, Phys. Lett. B **100**, 37 (1981).
- [96] A. D. Linde, Nucl. Phys. B **216**, 421 (1983), [Erratum: Nucl.Phys.B 223, 544 (1983)].
- [97] L. P. Csernai and J. I. Kapusta, Phys. Rev. D **46**, 1379 (1992).
- [98] R. Venugopalan and A. P. Vischer, Phys. Rev. E **49**, 5849 (1994), hep-ph/9307348.
- [99] J. E. McDonald, American Journal of Physics **30**, 870 (1962).
- [100] J. E. McDonald, American Journal of Physics **31**, 31 (1963).
- [101] V. Kalikmanov, Lecture Notes in Physics, Berlin Springer Verlag **860** (2013).
- [102] C. Caprini et al., JCAP **04**, 001 (2016), 1512.06239.
- [103] J. R. Espinosa, T. Konstandin, J. M. No, and G. Servant, JCAP **06**, 028 (2010), 1004.4187.
- [104] T. Konstandin and J. M. No, JCAP **02**, 008 (2011), 1011.3735.
- [105] M. Barroso Mancha, T. Prokopec, and B. Swiezewska, JHEP **01**, 070 (2021), 2005.10875.
- [106] S. Balaji, M. Spannowsky, and C. Tamarit, JCAP **03**, 051 (2021), 2010.08013.
- [107] W.-Y. Ai, B. Garbrecht, and C. Tamarit, JCAP **03**, 015 (2022), 2109.13710.
- [108] G. D. Moore and T. Prokopec, Phys. Rev. D **52**, 7182 (1995), hep-ph/9506475.
- [109] G. D. Moore and T. Prokopec, Phys. Rev. Lett. **75**, 777 (1995), hep-ph/9503296.
- [110] T. Konstandin, G. Nardini, and I. Rues, JCAP **09**, 028 (2014), 1407.3132.
- [111] J. Kozaczuk, JHEP **10**, 135 (2015), 1506.04741.
- [112] B. Laurent and J. M. Cline, Phys. Rev. D **102**, 063516 (2020), 2007.10935.
- [113] G. C. Dorsch, S. J. Huber, and T. Konstandin, JCAP **04**, 010 (2022), 2112.12548.
- [114] S. De Curtis, L. D. Rose, A. Guiggiani, A. G. Muyor, and G. Panico, JHEP **03**, 163 (2022), 2201.08220.
- [115] B. Laurent and J. M. Cline, Phys. Rev. D **106**, 023501 (2022), 2204.13120.
- [116] A. Adams, P. M. Chesler, and H. Liu, Science **341**, 368 (2013), 1212.0281.
- [117] A. Eichhorn, J. Lumma, J. M. Pawłowski, M. Reichert, and M. Yamada, JCAP **05**, 006 (2021), 2010.00017.
- [118] A. Kosowsky, M. S. Turner, and R. Watkins, Phys. Rev. D **45**, 4514 (1992).
- [119] A. Kosowsky, M. S. Turner, and R. Watkins, Phys. Rev. Lett. **69**, 2026 (1992).
- [120] A. Kosowsky and M. S. Turner, Phys. Rev. D **47**, 4372 (1993), astro-ph/9211004.
- [121] M. Kamionkowski, A. Kosowsky, and M. S. Turner, Phys. Rev. D **49**, 2837 (1994), astro-ph/9310044.
- [122] C. Caprini, R. Durrer, and G. Servant, Phys. Rev. D **77**, 124015 (2008), 0711.2593.
- [123] S. J. Huber and T. Konstandin, JCAP **09**, 022 (2008), 0806.1828.
- [124] C. Caprini, R. Durrer, T. Konstandin, and G. Servant, Phys. Rev. D **79**, 083519 (2009), 0901.1661.
- [125] D. J. Weir, Phys. Rev. D **93**, 124037 (2016), 1604.08429.
- [126] R. Jinno and M. Takimoto, Phys. Rev. D **95**, 024009 (2017), 1605.01403.

- [127] M. Hindmarsh, S. J. Huber, K. Rummukainen, and D. J. Weir, Phys. Rev. Lett. **112**, 041301 (2014), 1304.2433.
- [128] J. T. Giblin, Jr. and J. B. Mertens, JHEP **12**, 042 (2013), 1310.2948.
- [129] J. T. Giblin and J. B. Mertens, Phys. Rev. D **90**, 023532 (2014), 1405.4005.
- [130] M. Hindmarsh, S. J. Huber, K. Rummukainen, and D. J. Weir, Phys. Rev. D **92**, 123009 (2015), 1504.03291.
- [131] M. Hindmarsh, S. J. Huber, K. Rummukainen, and D. J. Weir, Phys. Rev. D **96**, 103520 (2017), [Erratum: Phys.Rev.D 101, 089902 (2020)], 1704.05871.
- [132] A. Kosowsky, A. Mack, and T. Kahniashvili, Phys. Rev. D **66**, 024030 (2002), astro-ph/0111483.
- [133] A. D. Dolgov, D. Grasso, and A. Nicolis, Phys. Rev. D **66**, 103505 (2002), astro-ph/0206461.
- [134] C. Caprini and R. Durrer, Phys. Rev. D **74**, 063521 (2006), astro-ph/0603476.
- [135] G. Gogoberidze, T. Kahniashvili, and A. Kosowsky, Phys. Rev. D **76**, 083002 (2007), 0705.1733.
- [136] T. Kahniashvili, L. Campanelli, G. Gogoberidze, Y. Maravin, and B. Ratra, Phys. Rev. D **78**, 123006 (2008), [Erratum: Phys.Rev.D 79, 109901 (2009)], 0809.1899.
- [137] T. Kahniashvili, L. Kisslinger, and T. Stevens, Phys. Rev. D **81**, 023004 (2010), 0905.0643.
- [138] C. Caprini, R. Durrer, and G. Servant, JCAP **12**, 024 (2009), 0909.0622.
- [139] L. Kisslinger and T. Kahniashvili, Phys. Rev. D **92**, 043006 (2015), 1505.03680.
- [140] J. Ellis, M. Lewicki, J. M. No, and V. Vaskonen, JCAP **06**, 024 (2019), 1903.09642.
- [141] T. Alanne, T. Hugle, M. Platscher, and K. Schmitz, JHEP **03**, 004 (2020), 1909.11356.
- [142] D. Cutting, M. Hindmarsh, and D. J. Weir, Phys. Rev. Lett. **125**, 021302 (2020), 1906.00480.
- [143] P. Binetruy, A. Bohe, C. Caprini, and J.-F. Dufaux, JCAP **06**, 027 (2012), 1201.0983.
- [144] A. H. Guth and S. H. H. Tye, Phys. Rev. Lett. **44**, 631 (1980), [Erratum: Phys.Rev.Lett. 44, 963 (1980)].
- [145] A. H. Guth and E. J. Weinberg, Phys. Rev. D **23**, 876 (1981).
- [146] M. D. Rintoul and S. Torquato, Journal of Physics A: Mathematical and General **30**, L585 (1997).
- [147] J. Liu, L. Bian, R.-G. Cai, Z.-K. Guo, and S.-J. Wang, Phys. Rev. D **105**, L021303 (2022), 2106.05637.
- [148] J. Shao and M. Huang (2022), 2209.13809.